3D Printed Mechanically Robust Graphene/CNT Electrodes for Highly Efficient Overall Water Splitting

Meiwen Peng, Danli Shi, Yinghui Sun, Jian Cheng, Bo Zhao, Yiming Xie, Junchang Zhang, Wei Guo, Zheng Jia,* Zhiqiang Liang,* and Lin Jiang*

3D printing of graphene electrodes with high mechanical strength has been a growing interest in the development of advanced energy, environment, and electronic systems, yet is extremely challenging. Herein, a 3D printed bioinspired electrode of graphene reinforced with 1D carbon nanotubes (CNTs) (3DP GC) with both high flexural strength and hierarchical porous structure is reported via a 3D printing strategy. Mechanics modeling reveals the critical role of the 1D CNTs in the enhanced flexural strength by increasing the friction and adhesion between the 2D graphene nanosheets. The 3DP GC electrodes hold distinct advantages: i) an intrinsically high flexural strength that enables their large-scale applications; and ii) a hierarchical porous structure that offers large surface area and interconnected channels, endowing fast mass and/or charge and ions transport rate, which is thus beneficial for acting as an ideal catalyst carrier. The 3DP GC electrode integrated with a NiFeP nanosheets array exhibits a voltage of 1.58 V at 30 mA cm^{-2} as bifunctional electrode for water splitting, which is much better than most of the reported Ni-, Co-, and Fe-based bifunctional electrocatalysts. Importantly, this study paves the way for the practical applications of 3D printed graphene electrodes in many energy conversion/storage, environmental, and electronic systems where high flexural strength is preferred.

The ever-growing demands for advanced energy, environment, and electronic techniques and devices have put forward pressing needs to high performance electrode. To this end, 3D electrodes have attracted considerable attentions due to high specific surface area and the resulting high loading capacity of active materials.[1–6] In particular, the emerging 3D graphene materials hold great potential as high-performance electrode due to their distinct advantages of high conductivity, excellent thermal and chemical stability, good biocompatibility, and abundant functional sites (e.g., absorption and/or activation sites).[7–11] Recently, extrusion-based 3D printing technique has been recognized as a promising way for fast and mass production of 3D graphene materials with hierarchical porous structure, such as the macroscaffold with micropores, which endows fast mass and/or charge and ions transport rate. So far, a variety of energy and electronic devices, such as lithium-ion batteries, supercapacitors, and sensors, have demonstrated significantly improved performances by applying 3D printed graphene electrodes compared with those based on traditional electrodes.[12–16] Note that 3D printed graphene electrodes have achieved good compression resistance and elasticity. This is because of that the multilayer 2D graphene nanosheets can effectively mutual support under compressive stress, and thus obtaining high strength and elastic stiffness.[12,17,18] Unfortunately, the low adhesion and friction between the 2D graphene nanosheets under tensile stress make the 3D printed graphene electrodes always end up with poor flexural strength, which seriously restrict their large-scale applications. As an example, the poor flexural strength of the traditional 3D printed graphene electrodes makes it easily to be broken under the bending force caused by surface tension and buoyancy of water, which is exactly the common stress situation that 3D printed graphene electrodes needed to be endured in many applications. Therefore, nowadays, there remains a pressing demand for 3D printed graphene electrodes with high flexural strength that are able to withstand the complex stress environment in their practical applications.

Inspired by the rows of 1D setae on gecko's feet, which act as strong bonding to gain high adhesive and friction between gecko's feet and the flat wall,[19,20] we design to construct mechanically robust 3D printed graphene electrodes

M. W. Peng, D. L. Shi, B. Zhao, Y. M. Xie, Dr. J. C. Zhang, W. Guo,
Prof. Z. Q. Liang, Prof. L. Jiang
Institute of Functional Nano and Soft Materials (FUNSOM)
Jiangsu Key Laboratory for Carbon-Based Functional Materials
and Devices and Joint International Research Laboratory
of Carbon-Based Functional Materials and Devices
Soochow University
Suzhou, Jiangsu 215123, P. R. China
E-mail: zqliang@suda.edu.cn; ljiang@suda.edu.cn
Prof. Y. H. Sun
College of Energy
Soochow Institute for Energy and Materials Innovations
Key Laboratory of Advanced Carbon Materials and Wearable Energy
Technologies of Jiangsu Province
Soochow University
Suzhou, Jiangsu 215006, P. R. China
Dr. J. Cheng
Department of Mechanical Engineering
University of Maryland College Park
College Park, MD 20742, USA
Prof. Z. Jia
Department of Engineering Mechanics
Zhejiang University
Hangzhou 310027, P. R. China
E-mail: zheng.jia@zju.edu.cn

The ORCID identification number(s) for the author(s) of this article can be found under https://doi.org/10.1002/adma.201908201.

DOI: 10.1002/adma.201908201
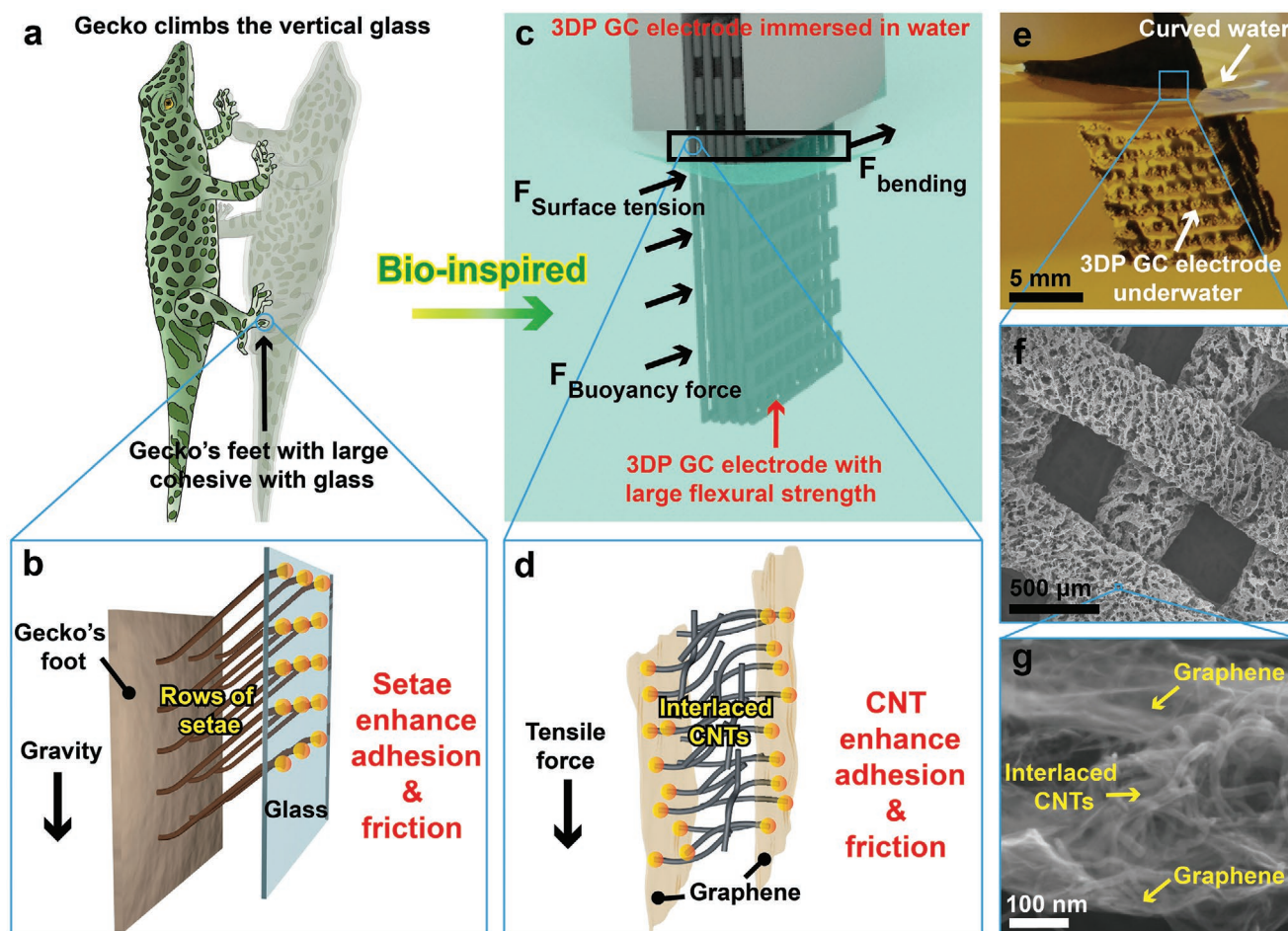
Figure 1. Gecko's feet-inspired design of 3DP GC electrode with high flexural strength. a,b) Schematically shown function of the rows of setae on gecko's feet that provides adequate bonding and friction between the gecko's feet and vertical glass. c,d) Schematic illustration shows 3DP GC electrode can withstand the large bending force caused by the surface tension and buoyancy when immersed in water because of the bioinspired graphene/interlaced CNTs nanostructure. e) Optical image of 3DP GC electrode immersed in water. f) SEM image of 3DP GC electrode with macroscaffold and microporous structure. g) SEM image of graphene/interlaced CNT nanostructure.

by incorporating 1D carbon nanotubes (CNTs) to reinforce the adhesion and friction among 2D graphene nanosheets (**Figure 1**a–d). The bioinspired 3D graphene/CNT electrodes with high flexural strength and hierarchical porous structure were built via an extrusion-based 3D printing approach and using the optimized partially reduced graphene oxide (pr-GO)/CNTs mixed ink. Mechanics modeling reveals the critical role of the CNTs in increasing friction between 2D graphene nanosheets, which is the key issue to achieve high biomimetic mechanical performance. As a result, the 3D printed graphene/CNT (3DP GC) electrode achieves a high flexural strength of 96.2 kPa, which enables it to readily withstand the bending force caused by surface tension and buoyancy when immersed in water (Figure 1c,e). Furthermore, the incorporation of 1D CNTs significantly enhances the conductivity of the printed 3D graphene electrodes (Figure S2, Supporting Information), which is also crucial to serving as high-performance electrodes. After in situ growth of NiFeP nanosheet arrays (NAs), the 24 layers of 3DP GC/NiFeP (3DP GC/NiFeP-24L) electrode exhibits overpotential of 133 mV (hydrogen evolution reaction (HER)) and 214 mV (oxygen evolution reaction (OER)) at a current of 30 mA cm^{-2} in 1.0 M KOH. Moreover, the 3DP GC/NiFeP-24L electrodes have voltage of 1.58 V at 30 mA cm^{-2} as both anode and cathode for water splitting. The good electrochemical performance stems from the conductive hierarchical porous structure of 3DP GC electrode, which is favorable for achieving uniformly 3D dispersion of NiFeP NA and facilitates efficient transport of electrons, ions, and gases. More importantly, the 3DP GC materials have great potential for a variety of energy conversion/storage, environment, and electronic applications where mechanically robust and hierarchical porous structures are in pressing demand.

In our previous work, 3D printed graphene materials achieved exceptionally high stiffness and resilience by simultaneously engineering macroscopic hollow structures and constructing cellular microstructure.[12] However, the poor flexural strength of the 3D printed graphene materials makes it easily to be broken under the bending force caused by large surface tension and buoyancy when they are immersed in water. Interestingly, some kinds of animals of Reptilia, such as gecko, have found their way to gained excellent ability to grasp the wall by evolving 1D setae structure on their flat feet (Figure 1a,b).

The rows of 1D setae of gecko's feet can act as strong bond, which endow high adhesion and friction between gecko's feet and the vertical wall. Inspired by this, the interlaced 1D CNTs are designed to reinforce the adhesion and friction between 2D graphene nanosheets (Figure 1c,d) and thus greatly improve the tensile strength of graphene/interlaced CNTs wall. As a result, the bioinspired 3DP GC electrode obtains significantly enhanced flexural strength, and thus holds the ability to avoid being broken when subjected to bending force. To realize the 3D printing of 1D CNTs reinforced 3D graphene materials, we optimized the aqueous-based graphene–CNTs mixed ink using the pr-GO[12] and the acidified CNT.[21] In the mixed ink, the mass ratio of CNT and pr-GO was kept at 3. Rheological properties characterizations (Figure S1, Supporting Information) reveal the high viscosity, significant shear-thinning behavior, and adequate modulus ($\approx 10^5$ Pa) of the pr-GO/CNT ink. The significant shear-thinning behavior makes the ink can be smoothly extruded from the fine nozzle, while the adequate G' endows the shape retention of extruded ink filaments. With the help of computer-aided programming, the direct extrusion-based printing route enables facile, fast, and scalable fabrication of complex 3D structures. After freeze-drying and high temperature annealing, porous microstructure is expected to be formed in the 3DP GC electrodes. Figure 1e shows that the 3DP GC electrode ($16 \times 10 \times 1.8$ mm³) can keep intact when immersed in water with an area of 10×10 mm², demonstrating adequate flexural strength. Additionally, this 3DP GC electrode features multiscale porous structure, 3D printed lattice macrostructure, and ice crystal extrusion induced porous microstructure (Figure 1f), which makes it has great potential to function as an electrocatalytic electrode. Figure 1g shows the biomimetic graphene/interlaced CNT nanostructure.

In order to reflect the distinct advantages of bioinspired graphene/interlaced CNTs nanostructure, 3DP graphene (3DP G) electrodes without incorporating 1D CNTs has also been printed as a comparison sample. As shown in **Figure 2**a–d, 3DP G electrodes has a microscopic porous structure similar to the 3DP GC electrode, however, the walls of 3DP G electrodes are formed by multilayer graphene, while the walls of 3DP GC are formed by bioinspired graphene/interlaced CNTs nanostructure. The 1D interlaced CNTs in the 3DP GC electrode are expected to significantly enhance the friction between the 2D graphene nanosheets and thus greatly improve the tensile strength of the graphene/interlaced CNTs wall. When the two electrodes are immersed in water with an area of 10×10 mm², 3DP G electrode is fractured under the bending force induced by surface tension and buoyancy due to its low bending strength, while the 3DP GC electrode remains intact in the same situation. (Figure 2e; Video S1, Supporting Information). Bending test (Figure 2f) reveals that the flexural stress of 3DP GC electrode is about four times that of 3DP G electrode. This result indicates that the bioinspired graphene/interlaced CNTs nanostructure endows the 3DP GC electrode with high flexural strength which allows it to avoid fracture when used as an electrocatalytic electrode in aqueous electrolyte. Additionally, 3DP GC electrode also displays much lower internal resistance and contact resistance than 3DP G electrode (Figure S2, Supporting Information), which is also in favor of its application as electrocatalytic electrode.

To further shed insight on the enhanced strength of the 3DP GC electrode, we compared the nanostructures of the 3DP GC and the 3DP G electrodes, and envisioned the following mechanistic understanding: the increase in strength essentially results from the bond breaking and significant friction between CNTs and graphene sheets. Figure 2g clarifies the envisioned strengthening mechanism of the 3DP GC electrode by illustrating models that are representative of the molecular-level deformation events in the 3DP GC and G electrodes. The 3DP GC electrode is comprised of interlaced CNT networks sandwiched by graphene sheets and is dense with CNT/graphene contacts. Under tension, the graphene sheets begin to slide against each other, and the pulling-off of these sheets eventually gives rise to the overall failure of the electrodes. We simulate the pulling out of a center graphene sheet from a nanostructure unit with three layers of graphene sheets (Figure 2g) by employing a cohesive-frictional model (Figure S3, Supporting Information). Figure 2h plots the interfacial energy dissipation of the simulation model as a function of the pulling out displacement. The results indicate that the breaking of CNT/graphene bonds and especially the subsequent friction due to relative sliding between CNTs and graphene sheets dissipate a significant amount of energy, and thus result in much enhanced strength (Figures S4–S6, Supporting Information). In stark contrast, the 3DP G electrodes do not contain CNTs, thereby lacking such a mechanism. Bonding between graphene sheets are negligible; the contacts between neighboring graphene sheets are less dense than the CNT/graphene contacts in the 3DP GC electrodes, such that the resultant frictional force in the 3DP G electrodes is much lower. To this end, pulling out a graphene sheet from the 3DP GC electrode dissipates much more energy than from the 3DP G electrode (Figure 2h), which explains the enhanced strength of the 3DP GC electrode compared with the 3DP G electrode. Furthermore, plotted in Figure S8 in the Supporting Information are the curves of flexural stress in 3DP GC electrodes as a function of the roller displacement, with various sample thickness (Figure S9, Supporting Information). It is revealed that the more layers in a sample, the thicker the electrode and the higher the fracture stress (the peak stress of the stress–deflection curve), indicating that increasing the sample thickness could effectively enhance its resistance to fracture.

Figure 3a schematically shows that the hierarchical porous structure of 3DP GC electrode could serve as an ideal support to the uniform loading of catalyst. As shown in Figure 3a–e, NiFeP NA was uniformly grown on the surface of a 24-layer-3DP GC electrode via hydrothermal reaction and phosphorization treatment. The 3DP GC/NiFeP electrode maintains the same macroscopic scaffold structure and microscopic porous structure as the 3DP GC electrode. It can be seen that the NiFeP NA grows uniformly on the cross-section of the 3DP GC electrode, which indicates that the interior (Figure S10, Supporting Information) of hierarchical porous 3DP GC electrode can function as loading site for NiFeP catalysts. Transmission electron microscopy (TEM) image further confirms that NiFeP nanosheets and graphene/CNT are combined together (Figure 3f). High-resolution TEM (HRTEM) characterization (Figure 3g) indicates the crystalline NiFeP with lattice fringe spaced at 0.221 nm, corresponding to 111 crystal plane of Ni_2P, which is consistent
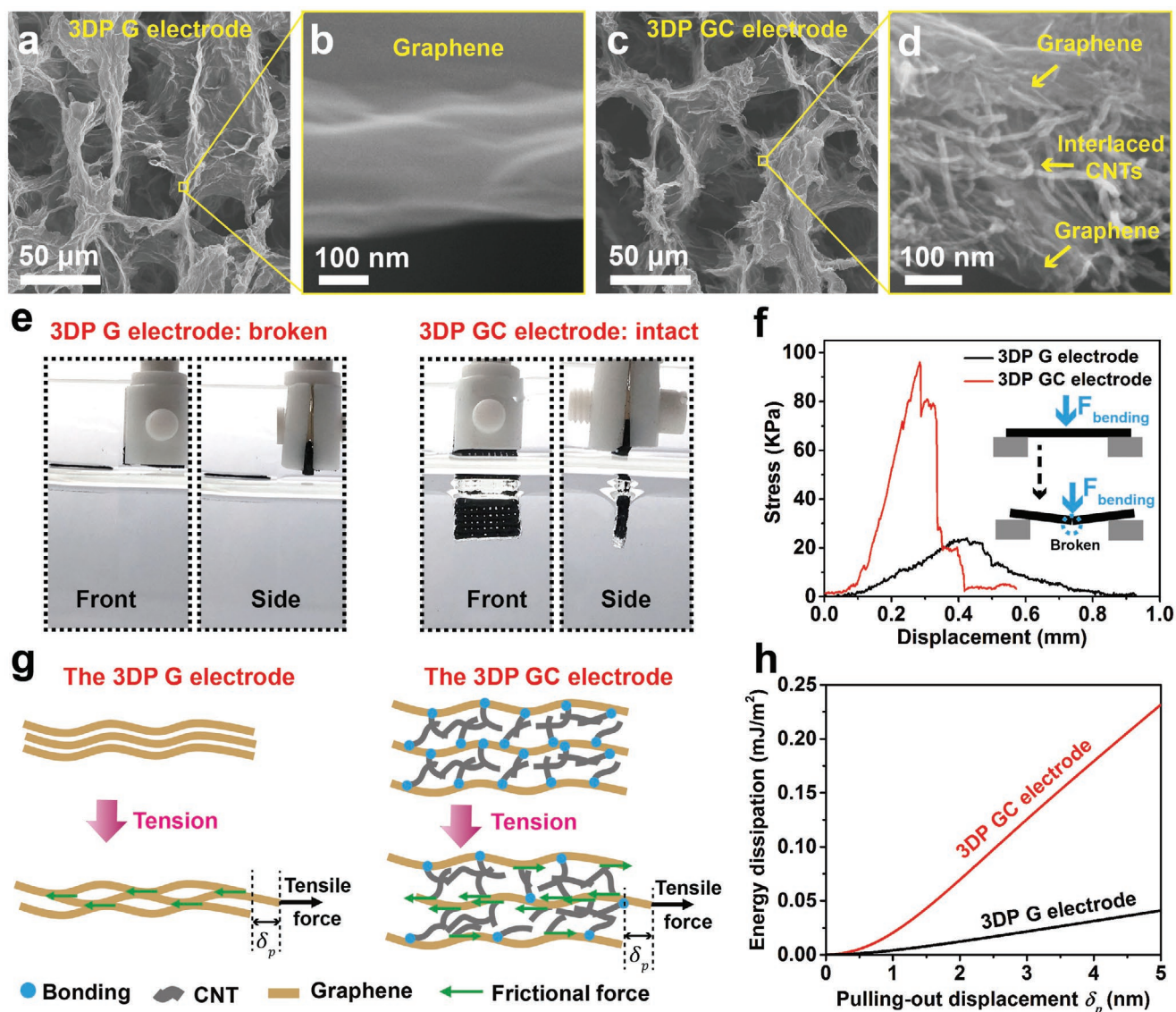
Figure 2. Comparison of structure and mechanical performance of 3DP G and 3DP GC electrodes. a–d) SEM images of 3DP-G (a,b) and 3DP-GC (c,d) electrodes. e) Optical images of 3DP G (left) and 3DP GC (right) electrodes in 1 M KOH aqueous electrolyte. f) Flexural stress as a function of roller displacement (bending deflection) for 3DP G and 3DP GC electrodes. The inset illustration presents the method of bending test. g) Envisioned molecular-level deformation mechanisms of the 3DP G and GC electrodes. h) Calculated energy dissipation as a function of the pulling-out displacement of a graphene nanosheet from 3DP G and GC electrodes.

with X-ray diffraction (XRD) characterization (Figure 3i). XRD pattern shows the diffraction peaks of 3DP GC/NiFeP basically consistent with that of the Ni_2P (JCPDS Card no. 74-1385) and FeP (JCPDS Card no. 78-1443), indicating NiFeP nanosheet is a mixture of Ni_2P and FeP. High-angle annular dark field scanning TEM (HAADF-STEM) and elemental mapping display the homogenous distribution of nickel, iron, and phosphorus over the NiFeP nanosheet (Figure 3i). X-ray photoelectron spectroscopy spectra further verify the existence of Ni, Fe, and P (Figure S11, Supporting Information). Ni 2p spectra analysis shows that the two obvious peaks at 857.6 and 875.4 eV can be attributed to Ni $2p_{3/2}$ and Ni $2p_{1/2}$. Fe 2p spectra analysis indicates that the two obvious peaks at 712.3 and 726.1 eV can be attributed to Fe $2p_{3/2}$ and Fe $2p_{1/2}$. In phosphorus spectrum,

the peak at 134.4 eV originates from PO_4^{3+}, and the subpeaks at 129.8 and 130.5 eV originates from P $2p_{3/2}$ and P $2p_{1/2}$.[22]

The high internal conductivity and hierarchical porous structure of 3DP GC/NiFeP electrodes make it very promising for highly efficient electron, ion and gas transport in HER and OER processes (**Figure 4**a). To fully exploit its catalytic performance, we investigated the HER and OER performance of the 3DP GC/NiFeP electrodes in 1.0 M KOH using a standard three-electrode system (Figure 4b). In addition, to clarify the role of the 3DP macroporous structure (millimeter-sized and interconnected channels), the bulk GC/NiFeP electrode and 12-layer-3DP GC/NiFeP (3DP GC/NiFeP-12) electrode with the same size were fabricated and characterized (Figure 4c–h; Figure S9, Supporting Information). The Tafel slopes of 3DP GC/NiFeP-12L
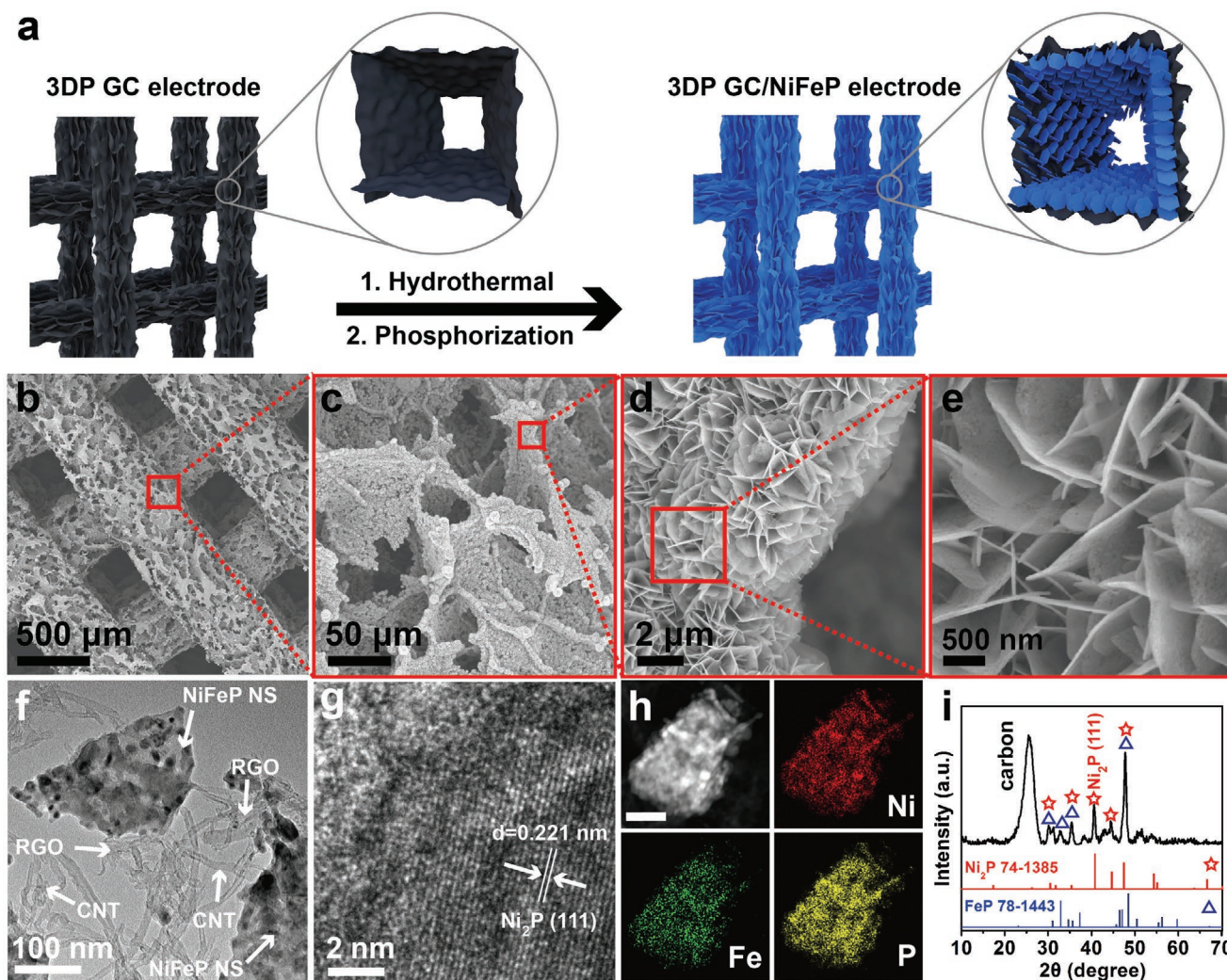
Figure 3. Morphology and composition characterization of 3DP GC/NiFeP electrode. a) Schematic diagram of the preparation process of NiFeP nanosheet arrays on 3DP GC electrode. b–e) SEM images of 3DP GC/NiFeP electrode. f) TEM image of NiFeP nanosheets combined together with CNT and RGO. g) HRTEM image of a NiFeP nanosheet. h) HAADF-STEM images of a NiFeP nanosheet and corresponding elemental mapping images of nickel, iron, and phosphorus. Scale bar: 100 nm. i) XRD pattern of 3DP GC/NiFeP electrode.

electrode in HER and OER are significantly lower than those of bulk GC/NiFeP electrode (Figure 4d,g). The driven overpotential to reach a current density of 30 mA cm^{-2} of 3DP GC/NiFeP-12L electrode is 182 mV (HER) and 270 mV (OER), which are smaller than 234 mV (HER) and 333 mV (OER) of bulk GC/NiFeP electrode (Figure 4e,h). Figure S12 in the Supporting Information shows the HER and OER polarization curves of 3DP GC/NiFeP-12L electrode and bulk GC/NiFeP electrode standardized by the amount of NiFeP. The standardized activity of 3DP GC/NiFeP-12L electrode is much higher than bulk GC/NiFeP electrode. The enhanced activity of 3DP GC/NiFeP-12L can be mainly attributed to the following two main reasons: i) a macroscopic scaffold structure with interconnected channels that can efficiently promotes the charge, ions, and gases transport; ii) a large surface area of microporous structure enables 3D dispersion of NiFeP and large contact area between NiFeP with electrolyte. Importantly, we suggest that this hierarchical porous 3DP GC also has great opportunities for loading many

other catalysts, such as noble metal nanoparticles, transition metal oxides and transition metal carbides, for promoting their practical applications in many energy conversion/storage, environmental and electronic systems where high flexural strength is preferred.

Additionally, the effects of electrode thickness on catalytic performance were further investigated. Thanks to the flexibility of extrusion-based 3D printing technique, we can precisely adjust the electrode thickness by controlling the layers of printed electrodes. As the thickness of the electrode increases, Tafel slope of HER and OER gradually decreases (Figure 4d,g). Similarly, the overpotential at a current of 30 and 100 mA cm^{-2} of HER and OER also becomes lower as the electrode thickness increases (Figure 4e,h). It is worth noting that the overpotential at a current of 30 mA cm^{-2} of our 3DP GC/NiFeP-24L is only 133 mV (HER) and 214 mV (OER), which is obviously lower than most of the reported Ni-, Co-, and Fe-based catalysts.[23–38] To demonstrate the advantages of 3DP GC electrodes over commercial carbon

**ADVANCED
SCIENCE NEWS**

www.advancedsciencenews.com

**ADVANCED
MATERIALS**

www.advmat.de
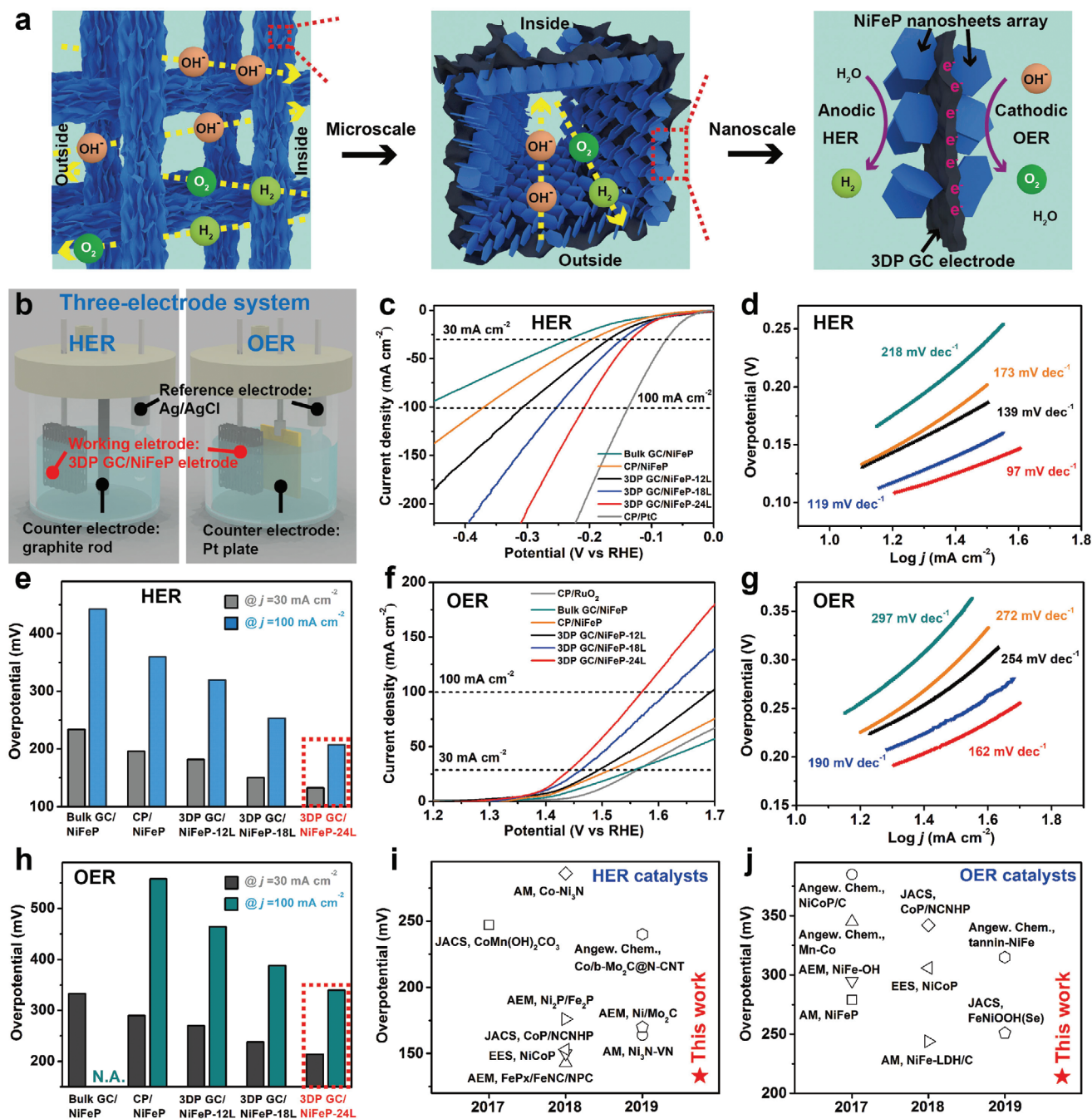
Figure 4. 3DP GC/NiFeP electrodes for HER and OER. a) Schematic diagram of the hierarchical porous structure of 3DP GC/NiFeP electrode facilitated ion and gas transport for both anode (HER) and cathode (OER) of water splitting. b) Schematic diagram of the three-electrode system. c) HER polarization curves, and d,e) corresponding Tafel plots (d), and overpotentials at current densities of 30 and 100 mA cm^{-2} (e) for 3DP GC/NiFeP electrodes with 12, 18, and 24 layers, bulk GC/NiFeP, and carbon paper (CP)/NiFeP electrodes. f) OER polarization curves, and g,h) corresponding Tafel plots (g) and overpotentials at current densities of 30 and 100 mA cm^{-2} (h) for 3DP GC/NiFeP electrodes with 12, 18, and 24 layers, bulk GC/NiFeP, and CP/NiFeP electrodes. i,j) Comparisons of overpotentials at a current density of 30 mA cm^{-2} for 3DP GC/NiFeP-24L with other HER catalysts[23–31] (i) and with other OER catalysts[26,27,32–38] (j) in the literature.

paper (CP), CP/NiFeP electrode was prepared and the HER and OER performance was tested (Figure 4c,f). Figure S13 in the Supporting Information shows that the NiFeP NA grows uniformly on the surface of the fibers of carbon paper, and its morphology is similar to that on the 3DP GC electrode. In order to fairly evaluate the performance advantage of 3DP GC electrode, we

further compared the activity of 3DP GC/NiFeP and CP/NiFeP electrodes with the standardized NiFeP loading at the same overpotential of 133 mV (HER) and 214 mV (OER) (Figure S14, Supporting Information). The current density of 3DP GC/NiFeP electrodes increases linearly and the corresponding mass activity of NiFeP remains unchanged with the enhancement of NiFeP

**ADVANCED
SCIENCE NEWS**

www.advancedsciencenews.com

**ADVANCED
MATERIALS**

www.advmat.de
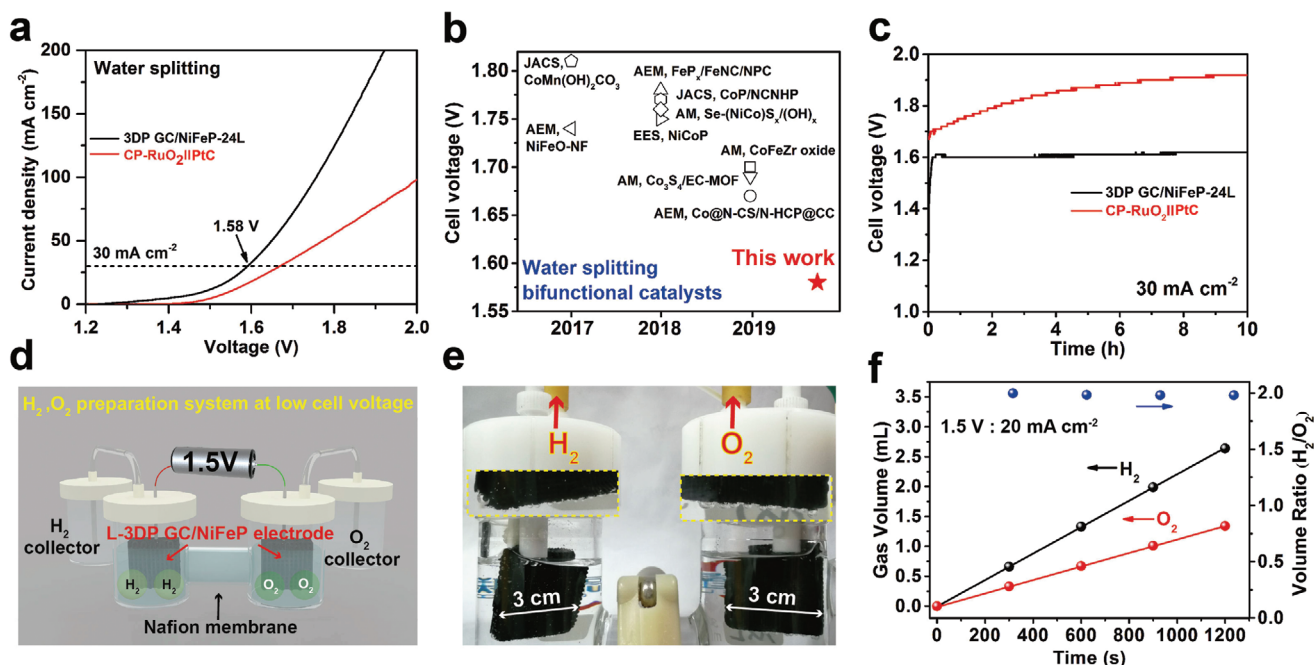
Figure 5. 3DP GC/NiFeP electrodes for water splitting. a) Two-electrode polarization curve of 3DP GC/NiFeP-24L electrodes (1×1 cm^2) for water splitting. b) Comparison of cell voltage at a current density of 30 mA cm^{-2} of 3DP GC/NiFeP-24L electrodes and bifunctional catalysts for water splitting in related reports in the literature.[23,24,26,27,39–43] c) Chronopotentiometric curve of 3DP GC/NiFeP-24L electrodes for two-electrode water splitting at 30 mA cm^{-2}. d) Schematic diagram of the H-type two-electrode water splitting system together with H$_2$ and O$_2$ collector using L-3DP GC/NiFeP electrodes (3×3 cm^2). e) Photograph of H-type two-electrode water splitting system and gas volume measurement by drainage. f) H$_2$ and O$_2$ evolution catalyzed by the L-3DP GC/NiFeP electrodes (3×3 cm^2).

loading (electrode thickness). In contrast, the current density of CP/NiFeP increases slowly and the corresponding mass activity of NiFeP decreases sharply with the enhancement of the NiFeP loading. These results indicate that our 3DP GC electrode can achieve high catalyst activity under high catalyst loading for HER and OER, which is significantly superior to the carbon paper. In addition, as a comparison, we have also prepared NiFeP on commercial Ni foam (NF) supporter and tested the HER and OER polarization curves of NF/NiFeP electrode (Figure S15, Supporting Information). Under the similar experimental condition, 3DP GC/NiFeP-24L electrode shows better HER and OER performance than NF/NiFeP electrode, which further prove the advantage of 3DP GC electrode.

Since the 3DP GC/NiFeP-24L electrode has both high HER and OER activity, we further employed it as both cathode and anode for a two-electrode water splitting cell. The cell requires a voltage as low as 1.58 V to achieve a current density of 30 mA cm^{-2}, which is superior to commercialized CP-RuO$_2$‖PtC (**Figure 5**a) and most of the reported bifunctional Ni-, Co-, and Fe-based electrocatalysts (Figure 5b).[23,24,26,27,39–43] Moreover, the 3DP GC/NiFeP-24L electrodes show excellent stability compared with the commercialized CP-RuO$_2$‖PtC (Figure 5c). Importantly, duo to the flexibility of 3D printing, we printed large (3×3 cm^2) 3DP GC-12L electrodes (Figure S16, Supporting Information) for water splitting, which evidences the ability of large-scale application of 3DP GC. After in situ growth of NiFeP NA, these large 3DP GC/NiFeP (L-3DP GC/NiFeP) electrodes are used as both cathode and anode for H$_2$, O$_2$ preparation system at 1.5 V (the voltage of a commercially available alkaline battery) (Figure 5d). The H-type electrolytic cell effectively

separates hydrogen and oxygen and collects them (Figure 5e). The current density of L-3DP GC/NiFeP at 1.5 V is 20 mA cm^{-2}, which is larger than 3DP GC/NiFeP-24L (1×1 cm^2). At the same time, the L-3DP GC/NiFeP electrodes generate 1.34 mL hydrogen and 2.64 mL oxygen in 1200 s, and the ratio of hydrogen to oxygen production is around 2 (Figure 5f; Video S2, Supporting Information).

In summary, we have printed mechanically robust 3DP GC electrodes via an extrusion-based 3D printing strategy. The significant enhancement in flexural strength finds its origin in the bioinspired graphene/interlaced CNTs nanostructure, which was proved by both experiments and simulations. The 3DP GC electrode synchronously satisfies high flexural strength, high conductivity, and hierarchical porous structure. After in situ growth of NiFeP NA, 3DP GC/NiFeP electrodes exhibit low cell voltage of 1.58 V at current density of 30 mA cm^{-2} and good cycle stability in water splitting as both cathode and anode. This bioinspired 3D printing of 1D nanomaterial reinforced 2D nanomaterials strategy is highly promising for fabricating various 3D structured materials with high mechanical property. More importantly, the 3DP GC materials have great potential for a variety of energy conversion/storage, environment, and electronic applications where mechanically robust and hierarchical porous structures are in pressing demand.

Supporting Information

Supporting Information is available from the Wiley Online Library or from the author.

Acknowledgements

Conflict of Interest

The authors declare no conflict of interest.

Keywords

[1] L. F. Chen, Y. Feng, H. W. Liang, Z. Y. Wu, S. H. Yu, *Adv. Energy Mater.* **2017**, *7*, 1700826.

[2] C. S. L. Koh, H. K. Lee, G. C. Phan-Quang, X. Han, M. R. Lee, Z. Yang, X. Y. Ling, *Angew. Chem., Int. Ed.* **2017**, *56*, 8813.

[3] H. Sun, J. Zhu, D. Baumann, L. Peng, Y. Xu, I. Shakir, Y. Huang, X. Duan, *Nat. Rev. Mater.* **2019**, *4*, 45.

[4] C. Wan, P. Cai, M. Wang, Y. Qian, W. Huang, X. Chen, *Adv. Mater.* **2019**, *31*, 1902434.

[5] J. C. Yang, J. Mun, S. Y. Kwon, S. Park, Z. Bao, S. Park, *Adv. Mater.* **2019**, *31*, 1904765.

[6] M. Dipalo, H. Amin, L. Lovato, F. Moia, V. Caprettini, G. C. Messina, F. Tantussi, L. Berdondini, F. De Angelis, *Nano Lett.* **2017**, *17*, 3932.

[7] S. Chowdhury, R. Balasubramanian, *Prog. Mater. Sci.* **2017**, *90*, 224.

[8] H. T. Sun, L. Mei, J. F. Liang, Z. P. Zhao, C. Lee, H. L. Fei, M. N. Ding, J. Lau, M. F. Li, C. Wang, X. Xu, G. L. Hao, B. Papandrea, I. Shakir, B. Dunn, Y. Huang, X. F. Duan, *Science* **2017**, *356*, 599.

[9] Y. Lu, Y. Ma, T. Zhang, Y. Yang, L. Wei, Y. Chen, *J. Am. Chem. Soc.* **2018**, *140*, 11538.

[10] N. Yousefi, X. Lu, M. Elimelech, N. Tufenkji, *Nat. Nanotechnol.* **2019**, *14*, 107.

[11] J. Lai, A. Nsabimana, R. Luque, G. Xu, *Joule* **2018**, *2*, 76.

[12] M. Peng, Z. Wen, L. Xie, J. Cheng, Z. Jia, D. Shi, H. Zeng, B. Zhao, Z. Liang, T. Li, L. Jiang, *Adv. Mater.* **2019**, *31*, 1902930.

[13] B. Yao, S. Chandrasekaran, J. Zhang, W. Xiao, F. Qian, C. Zhu, E. B. Duoss, C. M. Spadaccini, M. A. Worsley, Y. Li, *Joule* **2019**, *3*, 459.

[14] S. D. Lacey, D. J. Kirsch, Y. Li, J. T. Morgenstern, B. C. Zarket, Y. Yao, J. Dai, L. Q. Garcia, B. Liu, T. Gao, S. Xu, S. R. Raghavan, J. W. Connell, Y. Lin, L. Hu, *Adv. Mater.* **2018**, *30*, 1705651.

[15] K. Shen, H. L. Mei, B. Li, J. W. Ding, S. B. Yang, *Adv. Energy Mater.* **2018**, *8*, 1701527.

[16] Q. Zhang, F. Zhang, X. Xu, C. Zhou, D. Lin, *ACS Nano* **2018**, *12*, 1096.

[17] D. A. Dikin, S. Stankovich, E. J. Zimney, R. D. Piner, G. H. Dommett, G. Evmenenko, S. T. Nguyen, R. S. Ruoff, *Nature* **2007**, *448*, 457.

[18] H. L. Gao, Y. B. Zhu, L. B. Mao, F. C. Wang, X. S. Luo, Y. Y. Liu, Y. Lu, Z. Pan, J. Ge, W. Shen, Y. R. Zheng, L. Xu, L. J. Wang, W. H. Xu, H. A. Wu, S. H. Yu, *Nat. Commun.* **2016**, *7*, 12920.

[19] K. Autumn, Y. A. Liang, S. T. Hsieh, W. Zesch, W. P. Chan, T. W. Kenny, R. Fearing, R. J. Full, *Nature* **2000**, *405*, 681.

[20] K. Autumn, M. Sitti, Y. A. Liang, A. M. Peattie, W. R. Hansen, S. Sponberg, T. W. Kenny, R. Fearing, J. N. Israelachvili, R. J. Full, *Proc. Natl. Acad. Sci. USA* **2002**, *99*, 12252.

[21] J. C. Sun, P. D. Li, J. Y. Qu, X. Lu, Y. Q. Xie, F. Gao, Y. Li, M. F. Gang, Q. J. Feng, H. W. Liang, X. C. Xia, C. R. Li, S. C. Xu, J. M. Bian, *Nano Energy* **2019**, *57*, 269.

[22] R. Q. Li, B. L. Wang, T. Gao, R. Zhang, C. Y. Xu, X. F. Jiang, J. J. Zeng, Y. Bando, P. F. Hu, Y. L. Li, X. B. Wang, *Nano Energy* **2019**, *58*, 870.

[23] T. Tang, W. J. Jiang, S. Niu, N. Liu, H. Luo, Y. Y. Chen, S. F. Jin, F. Gao, L. J. Wan, J. S. Hu, *J. Am. Chem. Soc.* **2017**, *139*, 8320.

[24] Q. Qin, H. Jang, P. Li, B. Yuan, X. Liu, J. Cho, *Adv. Energy Mater.* **2019**, *9*, 1803312.

[25] C. Zhu, A. L. Wang, W. Xiao, D. Chao, X. Zhang, N. H. Tiep, S. Chen, J. Kang, X. Wang, J. Ding, J. Wang, H. Zhang, H. J. Fan, *Adv. Mater.* **2018**, *30*, 1705516.

[26] E. Hu, Y. Feng, J. Nai, D. Zhao, Y. Hu, X. Lou, *Energy Environ. Sci.* **2018**, *11*, 872.

[27] Y. Pan, K. Sun, S. Liu, X. Cao, K. Wu, W. C. Cheong, Z. Chen, Y. Wang, Y. Li, Y. Liu, D. Wang, Q. Peng, C. Chen, Y. Li, *J. Am. Chem. Soc.* **2018**, *140*, 2610.

[28] Y. C. Ge, P. Dong, S. R. Craig, P. M. Ajayan, M. X. Ye, J. F. Shen, *Adv. Energy Mater.* **2018**, *8*, 1800484.

[29] M. X. Li, Y. Zhu, H. Y. Wang, C. Wang, N. Pinna, X. F. Lu, *Adv. Energy Mater.* **2019**, *9*, 1803185.

[30] T. Ouyang, Y. Ye, C. Wu, K. Xiao, Z. Liu, *Angew. Chem., Int. Ed.* **2019**, *58*, 4923.

[31] H. Yan, Y. Xie, A. Wu, Z. Cai, L. Wang, C. Tian, X. Zhang, H. Fu, *Adv. Mater.* **2019**, *31*, 1901174.

[32] P. He, X. Yu, X. Lou, *Angew. Chem., Int. Ed.* **2017**, *56*, 3897.

[33] B. Y. Guan, L. Yu, X. W. Lou, *Angew. Chem., Int. Ed.* **2017**, *56*, 2386.

[34] W. Zhang, Y. Z. Wu, J. Qi, M. X. Chen, R. Cao, *Adv. Energy Mater.* **2017**, *7*, 1602547.

[35] F. Hu, S. Zhu, S. Chen, Y. Li, L. Ma, T. Wu, Y. Zhang, C. Wang, C. Liu, X. Yang, L. Song, X. Yang, Y. Xiong, *Adv. Mater.* **2017**, *29*, 1606570.

[36] S. Yin, W. Tu, Y. Sheng, Y. Du, M. Kraft, A. Borgna, R. Xu, *Adv. Mater.* **2018**, *30*, 1705106.

[37] Y. Shi, Y. Yu, Y. Liang, Y. Du, B. Zhang, *Angew. Chem., Int. Ed.* **2019**, *58*, 3769.

[38] S. Niu, W. J. Jiang, Z. Wei, T. Tang, J. Ma, J. S. Hu, L. J. Wan, *J. Am. Chem. Soc.* **2019**, *141*, 7005.

[39] C. Q. Dong, T. Y. Kou, H. Gao, Z. Q. Peng, Z. H. Zhang, *Adv. Energy Mater.* **2018**, *8*, 1701347.

[40] C. Hu, L. Zhang, Z. J. Zhao, A. Li, X. Chang, J. Gong, *Adv. Mater.* **2018**, *30*, 1705538.

[41] T. Liu, P. Li, N. Yao, T. Kong, G. Cheng, S. Chen, W. Luo, *Adv. Mater.* **2019**, *31*, 1806672.

[42] L. Huang, D. Chen, G. Luo, Y. R. Lu, C. Chen, Y. Zou, C. L. Dong, Y. Li, S. Wang, *Adv. Mater.* **2019**, *31*, 1901439.

[43] Z. Chen, Y. Ha, H. Jia, X. Yan, M. Chen, M. Liu, R. Wu, *Adv. Energy Mater.* **2019**, *9*, 1803918.